TOPICAL REVIEW — Iron-based high temperature superconductors

Molecular beam epitaxy and superconductivity of stoichiometric FeSe and $K_xFe_{2-y}Se_2$ crystalline films*

Wang Li-Li(王立莉)[a], Ma Xu-Cun(马旭村)[a], Chen Xi(陈 曦)[b], and Xue Qi-Kun(薛其坤)[b]†

[a] Institute of Physics, Chinese Academy of Sciences, Beijing 100190, China

[b] State Key Laboratory of Low-Dimensional Quantum Physics, Department of Physics, Tsinghua University, Beijing 100084, China

(Received 3 May 2013)

Our recent progress in the fabrication of FeSe and $K_xFe_{2-y}Se_2$ ultra thin films and the understanding of their superconductivity properties is reviewed. The growth of high-quality FeSe and $K_xFe_{2-y}Se_2$ films is achieved in a well controlled manner by molecular beam epitaxy. The high-quality stoichiometric and superconducting crystalline thin films allow us to investigate the intrinsic superconductivity properties and the interplay between the superconductivity and the film thickness, the local structure, the substrate, and magnetism. *In situ* low-temperature scanning tunneling spectra reveal the nodes and the twofold symmetry in FeSe, high-temperature superconductivity at the FeSe/$SrTiO_3$ interface, phase separation and magnetic order in $K_xFe_{2-y}Se_2$, and the suppression of superconductivity by twin boundaries and Fe vacancies. Our findings not only provide fundamental information for understanding the mechanism of unconventional superconductivity, but also demonstrate a powerful way of engineering superconductors and raising the transition temperature.

Keywords: superconducting films, Fe-based superconductors, molecular beam epitaxy, scanning tunneling microscopy

PACS: 68.37.Ef, 68.55.Jk, 74.78.Bz **DOI:** 10.1088/1674-1056/22/8/086801

1. Introduction

One of the most active areas of research in condensed matter physics at present is iron-based high critical temperature (T_C) superconductivity. The iron-based superconductors consist of FeAs[1–7] or FeSe[8–20] layers, which are widely believed to be the key component of their novel superconductivity properties, similar to the CuO_2 layers in high T_C cuprates. Those with FeAs layers, iron pnictides, usually have a higher T_C than those with FeSe layers, iron chalcogides. So far, the recorded critical temperature T_C in Fe-based superconductors is 55 K for SmFeAsO.[4] PbO-type β-FeSe is a typical example of iron chalcogides. It superconducts, although at a lower T_C of 8 K,[8] and has a simpler structure than the pnictides. The critical temperature can be dramatically increased by Te substitution, or even more by pressure up to 37 K.[9,10] FeSe shows several similarities to iron pnictide superconductors,[7,17] which include the common structural motif of the FeX_4 (X = Se, As, P) tetrahedral (the iron cations are tetrahedrally coordinated locally to Se as in $FeAs_4$), similar band filling, and low-temperature structure distortion from tetragonal to orthorhombic crystal symmetry. The similarities, together with its simple chemical formula and crystallographic structure, make FeSe a prototype system for unraveling the mechanism of superconductivity in all iron-based superconductors. Moreover, the recent developments of compounds with chemical formulas $A_xFe_{2-y}Se_2$ (A = alkali element)[21–33] show superconductivity at temperatures comparable to those of the pnictides, for example $T_C = 33$ K[32] for $K_{0.8}Fe_2Se_2$. Unlike the case of iron pnictide superconductors, where the parent magnetic compounds are metallic, $K_xFe_{2-y}Se_2$ has a magnetic insulating ground state, potentially bringing the fields of the Fe superconductors and the Cu superconductors closer.

Two central issues in studying quantum materials are the quality of the samples and the sensitivity of the experimental probes. Molecular beam epitaxy (MBE) is one of the most powerful techniques for the growth of thin films with precisely controlled composition and crystalline quality. Besides, atomic defects with controlled density can be delicately controlled by growth conditions and post annealing. Scanning tunneling microscopy/spectroscopy (STM/STS) can reveal the surface structure and morphology with atomic resolution, and can also probe the local density of state (DOS) with an energy range up to several eV near the Fermi level (E_F) with tunneling conductance spectra (dI/dV). STS has been used to reveal the local superconducting gap and defect-induced subgap states in superconductors.[34–36] By taking the tunneling conductance spectra at a given energy at different spatial locations in real space, the spatial variation of the sample DOS can also be extracted. This DOS mapping technique has been applied to measure the local gap variations and magnetic vortices.[37,38] We have employed MBE-STM

*Project supported by the National Natural Science Foundation of China and the National Basic Research Program of China.

†Corresponding author. E-mail: qkxue@mail.tsinghua.edu.cn

© 2013 Chinese Physical Society and IOP Publishing Ltd

combined systems to study the superconductivity properties of two-dimensional superconducting films.

In this paper, we review our recent progress in understanding the superconductivity properties of FeSe and $K_xFe_{2-y}Se_2$ ultra thin films grown by MBE. The growth of high-quality FeSe and $K_xFe_{2-y}Se_2$ films is achieved in a well controlled manner under Se-rich growth conditions. The superconductivity properties are studied by probing the quasiparticle density of states and measuring the superconducting gap at E_F using STM/STS. The organization of the review is as follows. In Section 2, the molecular beam epitaxial growth of superconducting FeSe and $K_xFe_{2-y}Se_2$ films is presented,[39–43] with information on the growth conditions and film morphology. In Section 3, the superconductivity properties of FeSe films on graphitized SiC (0001) substrate,[39,40] hereafter called substrate graphene/SiC, are discussed. We show the pairing symmetry and the influences of film thickness and local structure. In Section 4, we summarize the results of single unit cell (UC) thick FeSe films on $SrTiO_3$ (STO) (001) substrate,[41] and discuss the possible mechanism of the interface-enhanced superconductivity. In Section 5, the superconductivity properties of $K_xFe_{2-y}Se_2$ films on graphene/SiC[42] and STO (001)[43] substrates are reviewed, with an emphasis on the phase separation, one of the central issues in this material.

2. Molecular beam epitaxial growth of FeSe and $K_xFe_{2-y}Se_2$ films

The uncertainty in the stoichiometry of Fe(Se,Te) samples[8,10,17] has made it challenging to understand the superconducting and normal states in the materials. To avoid this complexity, we grew the stoichiometric FeSe and $K_xFe_{2-y}Se_2$ single-crystalline films using MBE. Growth was carried out in a standard MBE chamber with a base pressure of 10^{-10} Torr (1 Torr = 1.33322×10^2 Pa). High-purity Fe (99.995%) and Se (99.999%) were used as the source materials. FeSe films were grown by co-evaporating Fe and Se sources from standard Knudsen cells, and $K_xFe_{2-y}Se_2$ films by ternary co-evaporation with an additional K source from an alkali-metal dispenser. Due to the very volatile nature of Se molecules, a high Se/Fe flux ratio of > 10 was used to compensate for the Se loss. For optimal substrate temperature (the temperature of the substrate (T_{sub}) is set between the cell temperature of Se (T_{Se}) and that of Fe (T_{Fe}), that is, $T_{Fe} \gg T_{sub} > T_{Se}$), the stoichiometry of the films is self-regulating: the extra Se atoms cannot be incorporated into the FeSe films since the substrate temperature is higher than the sublimation temperature of Se. Under these conditions, the growth rate is linearly dependent on the Fe flux determined by T_{Fe}. The Se-rich conditions ensure almost Se vacancy-free samples with very high crystalline quality. To remove the extra Se (K) adatoms and obtain the superconducting phase, the samples were annealed at ~ 400 °C for several hours after growth.

The FeSe films that are epitaxial on graphene/SiC and STO (001) substrates both have an Se-terminated (001) surface, and growth is basically in a layer-by-layer mode. Figure 1 shows typical STM topographic images of the FeSe films, with a thickness of 30 UC, grown on graphene/SiC substrate at 450 °C. The temperatures of the Fe-cell and Se-cell were 1150 °C and 136 °C, respectively, which leads to a growth rate of 0.13 UC/min. The STM topographic images reveal atomically flat and defect-free Se-terminated (001) surfaces with large terraces. Each bright spot in the STM image corresponds to an apical Se atom above the Fe plane. The selenium atom spacing (Fig. 1(b)) in the topmost layer is 3.8 Å, which matches that of bulk β-FeSe well. Figure 2 shows typical STM topographic images of 1-UC thick FeSe films grown on Se-etched STO (001) substrate at 450 °C. The STM topographic image in Fig. 2(a) shows the atomically flat surface with domains. The atomic-resolution image in Fig. 2(b) reveals a perfectly ordered Se-terminated (001) lattice with an in-plane lattice constant of 3.8 Å, the same as that of FeSe grown on graphene/SiC (0001).

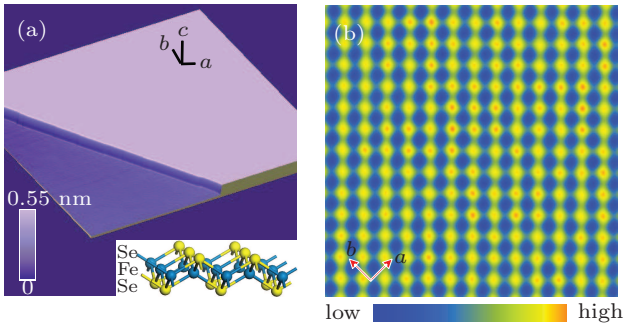


Fig. 1. STM topography of FeSe films on graphene/SiC. (a) Topographic image of an FeSe film; the step height is 5.5 Å. The inset shows the crystal structure. (b) Atomic-resolution STM topography of the FeSe film.

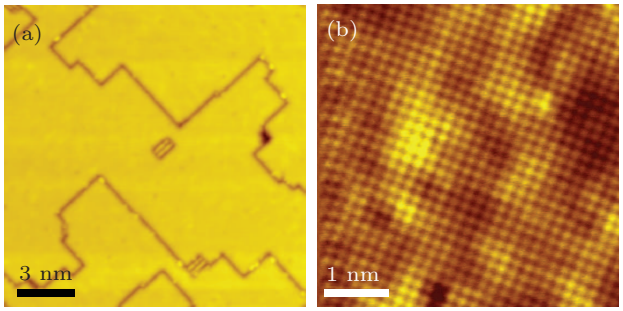


Fig. 2. STM topography of FeSe films on STO (001). (a) STM topography showing the grain boundaries, and (b) atomic resolution STM topography showing the Se-terminated FeSe (001) lattice.

$K_xFe_{2-y}Se_2$ films that are epitaxial on graphene/SiC substrate are (110) oriented, while those on STO (001) substrate

are (001) oriented. In Fig. 3, we show STM topographic images of $K_xFe_{2-y}Se_2$ films on graphene/SiC. The island size is typically 100 nm×100 nm. Two distinct regions, marked by I and II in Fig. 3(a), coexist side-by-side on each island. The atomic-resolution STM image of region I (Fig. 3(b)) exhibits a centered rectangular lattice structure. The periods along the two orthogonal directions are 5.5 Å and 14.1 Å, respectively, suggesting the (110) orientation terminated with K and Se atoms. The K atoms are visible under a positive bias and form atomic rows (Fig. 3(b)), which are 7.05 Å apart and oriented along the $[1\bar{1}0]$ direction. Under a negative bias, the Se atomic rows (indicated by black dots in Fig. 3(c)) appear and zigzag through the K atoms. Furthermore, there are very few defects in region I. We therefore identify region I as stoichiometric KFe_2Se_2. Figure 3(d) shows the atomic-resolution STM image of region II. Besides the K atomic rows in the topmost layer, there is a superimposed striped structure along the c axis, perpendicular to the K atomic rows. The period of the superimposed striped structure is 14.0 Å ($\sim 5a_{Fe}$), where a_{Fe} is the in-plane distance between two neighboring Fe atoms. We attribute this superstructure to the $\sqrt{5}\times\sqrt{5}$ pattern of Fe vacancies in the second atomic layer. They are visible in the STM images because the electronic structure of the topmost layer is perturbed by the missing Fe–Se bonds. The $\sqrt{5}\times\sqrt{5}$ vacancy order leads to a composition of $K_2Fe_4Se_5$ or $K_{2.5}Fe_4Se_5$.

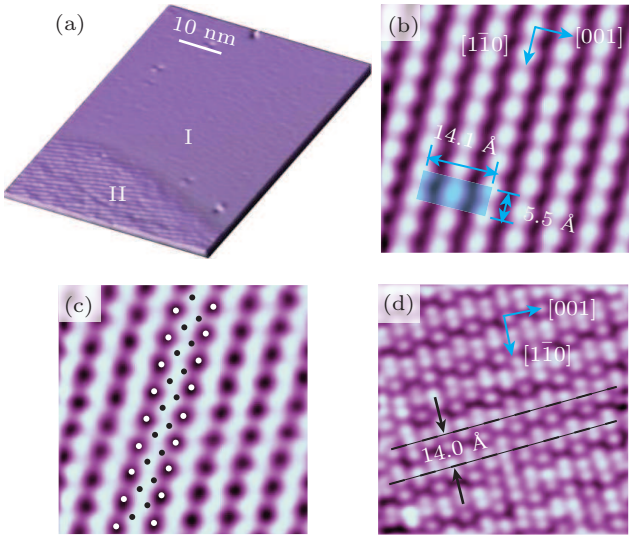


Fig. 3. STM topography of $K_xFe_{2-y}Se_2$ films on graphene/SiC. (a) Topographic image showing two distinct regions, labeled I and II (3.9 V, 0.02 nA). (b), (c) Atomic-resolution STM topography of region I. The two images show the same area, but with different bias voltages: 0.15 V for (b) and −2 V for (c). (d) Atomic-resolution STM topography of region II (2.9 V, 0.02 nA).

In Fig. 4, we show the STM topographic images of $K_xFe_{2-y}Se_2$ films on STO (001) substrate. According to the atomic-resolution STM image acquired at a sample bias of −90 mV (Fig. 4(a)), the film surface has a square lattice of 3.9 Å×3.9 Å, suggesting the (001) plane of a stoichiometric KFe_2Se_2 single-crystalline film without reconstruction. However, inhomogeneity in the electronic structure is clearly revealed by the atomically resolved STM image of the same area at a positive sample bias of 50 mV. As shown in Fig. 4(b), the film contains two regions labeled I and II, and the 1×1-Se square lattice is uninterrupted at the boundary of the two regions (Fig. 4(a)). At a bias voltage within ±100 mV, region I exhibits a $\sqrt{2}\times\sqrt{2}$ superstructure with respect to the original Se lattice (Fig. 4(c)). At a bias voltage within ±60 mV, region II exhibits a fret-like pattern, which breaks the fourfold symmetry (Fig. 4(d)) with a basic building block of $\sqrt{2}\times\sqrt{5}$ charge density modulation (the parallelogram in the inset). The region is divided into domains depending on the orientations of the stripes.

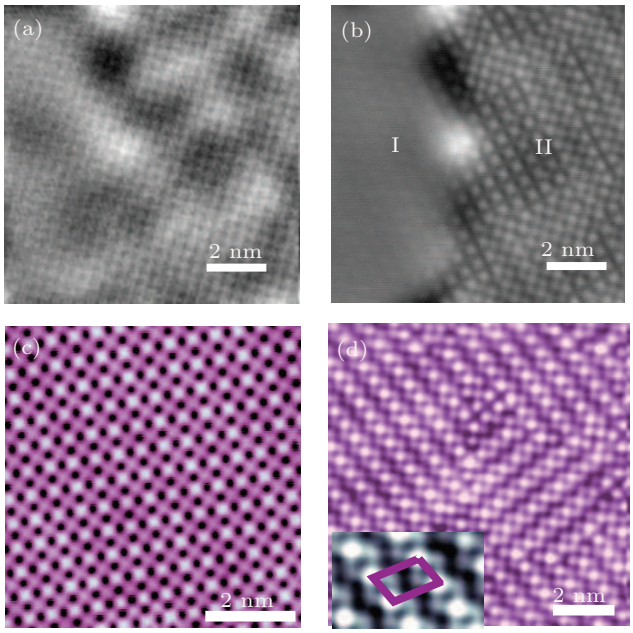


Fig. 4. STM topography of $K_xFe_{2-y}Se_2$ films on STO (001). (a), (b) Atomic-resolution STM topography of KFe_2Se_2. The two images show the same area, but with different bias voltages: −90 mV for (a) and 50 mV for (b). (c) The $\sqrt{2}\times\sqrt{2}$ charge ordering in region I (40 mV, 0.02 nA). (d) The $\sqrt{2}\times\sqrt{5}$ charge ordering (also see inset) in region II (30 mV, 0.02 nA).

The stoichiometric KFe_2Se_2 in regions I and II has the same crystal structure but exhibits very different electronic properties. We attribute the difference to the existence of an antiferromagnetic $K_2Fe_4Se_5$ insulating layer below the KFe_2Se_2 film in region II (see the schematic in Fig. 5(a)). Although the $K_2Fe_4Se_5$ layer is a few nanometers below the surface, its $\sqrt{5}\times\sqrt{5}$ Fe vacancy order is still visible in an STM image at 70 mV (Fig. 5(b)) due to the three-dimensional tunneling effect.[44] The dashed circles in Fig. 5(b) highlight some of the atoms forming the $\sqrt{5}\times\sqrt{5}$ pattern. The existence of the $K_2Fe_4Se_5$ layer below KFe_2Se_2 is further supported by the well-defined Moire pattern marked by arrows. The period of the pattern is $3\sqrt{5}a_{Se}$, where a_{Se} is the Se–Se distance. The

Moire pattern is in excellent agreement with a simple simulation (supplemental material in Ref. [43]), where two lattices with $\sqrt{2}\times\sqrt{5}$ and $\sqrt{5}\times\sqrt{5}$ superstructures are superimposed.

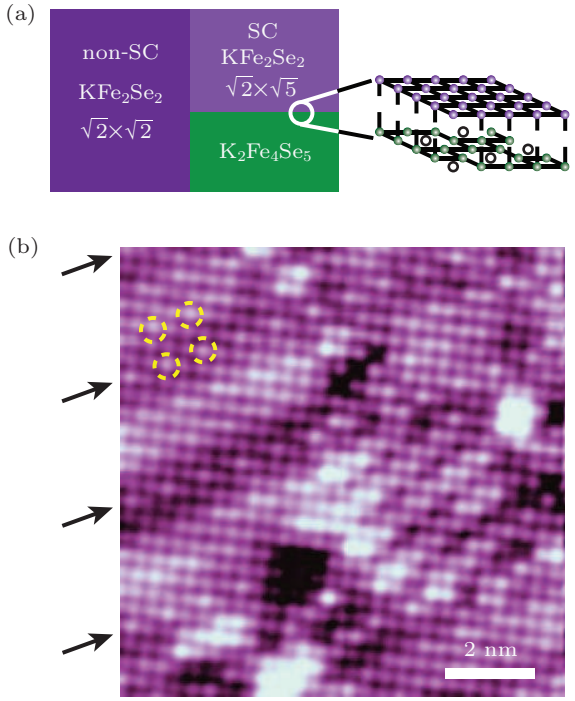


Fig. 5. The relationship between insulating $K_2Fe_4Se_5$ and superconducting KFe_2Se_2. (a) Schematic diagram. Across the interface between KFe_2Se_2 and $K_2Fe_4Se_5$, the lattice structure is the same except for a $\sqrt{5}\times\sqrt{5}$ Fe vacancy order in $K_2Fe_4Se_5$. (b) The $\sqrt{5}\times\sqrt{5}$ superstructure in region II of Fig. 4(b). The image belongs to the same area as Fig. 4(d), but with a different bias voltage (70 mV). The Moire pattern is marked by arrows.

3. Superconductivity properties of FeSe films on graphene/SiC substrate

Here, a chemically inert double-layer graphene formed on SiC (0001) is used as the substrate. The advantage of this approach is that the interaction of the FeSe film with the underlying substrate is rather weak, so that FeSe almost "floats" on the double-layer graphene and no strain results in the FeSe films. STM observation of ultrathin FeSe films (1–4 UC) reveals that they have the same lattice constant as the thick films and bulk β-FeSe, suggesting a fully relaxed FeSe film even at the first UC. Thus, the superconductivity properties of the FeSe films should be similar to those of bulk FeSe.

3.1. Direct observation of nodes and twofold symmetry

Figure 6 shows the tunneling spectra of the sample in Fig. 1(a) at various temperatures. At a temperature below T_C, the spectra exhibit two conductance peaks and a gap centered at the Fermi energy. The maximum of the superconducting gap $\Delta_0 = 2.2$ meV is half of the energy between the two conductance peaks. The most striking feature of the spectra at 0.4 K, analogous to the cuprate high-T_C superconductors,[37] is the V-shaped $\mathrm{d}I/\mathrm{d}V$ and the linear dependence of the quasiparticle density of states on energy near E_F. This feature explicitly reveals the existence of line nodes in the superconducting gap function. At elevated temperatures, the V-shaped spectra smear out as the superconducting gap disappears above T_C.

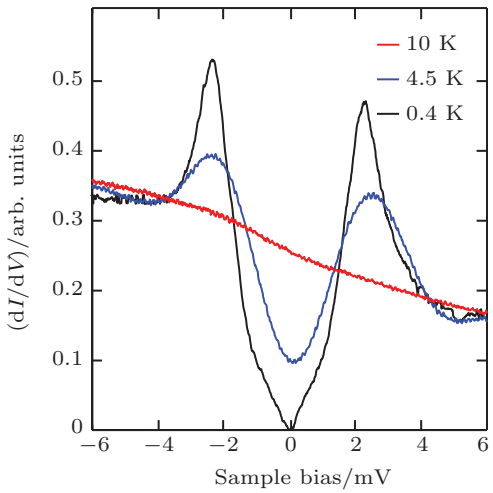


Fig. 6. The temperature dependence of the tunneling conductance spectra in 30-UC FeSe films on graphene/SiC (10 mV, 0.1 nA).

When a magnetic field is applied (perpendicularly) to the FeSe sample surface, the field can enter the superconductor in the form of vortices. The superconducting order parameter is zero at the center of the vortex and approaches the zero-field value at a distance on the order of the coherence length ξ. The $\mathrm{d}I/\mathrm{d}V$ curve at the center of the vortex in FeSe shows a pronounced zero-bias peak (Fig. 7(a)) that originates from quasiparticle bound states. The spatial distribution of the peak reflects the quasiparticle wave function and is mapped out by measuring $\mathrm{d}I/\mathrm{d}V$ at zero bias in the vicinity of a single vortex (Fig. 7(b)). This resonance state elongates along the a axis (presumably a direction with nodes). Away from the center of the vortex core, the resonance peak splits into two symmetric branches in energy (Figs. 7(c) and 7(d)). Although the peaks along the b axis eventually merge into the gap edges at a distance of 20 nm from the center (Fig. 7(d)), the energy of the peaks along the a axis approaches ± 0.6 meV instead of $\Delta_0 = 2.2$ meV (Fig. 7(c)).

The twofold symmetry of the FeSe gap function is further supported by the impurity-induced resonance states inside the superconducting gap. We deposited Fe atoms on the FeSe surface at a low temperature (50 K). Single Fe adatoms formed and occupied the hollow sites of the surface Se lattice (Fig. 8(a)). On an Fe adatom, two resonance states at -1.4 meV and -0.4 meV were clearly observed (Fig. 8(b)). The DOS map in Fig. 8(c) again shows the twofold symmetry, but the state is more visible in the direction perpendicular to the long axis of the vortex core. Similar spectra and density of states maps were also observed on Se vacancies (Figs. 8(d)–8(f)). Intuitively, the anisotropic distribution of the core state can be understood by the difference between coherence lengths ξ along the a and b directions, a phenomenon which mainly stems from the twofold symmetry of the gap function.

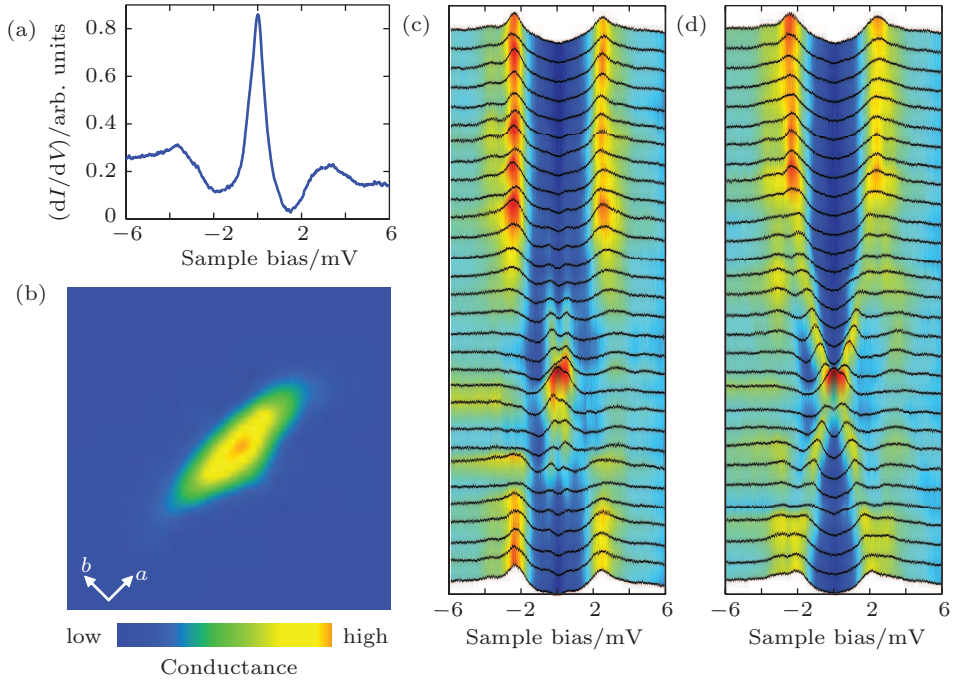


Fig. 7. Vortex core states in FeSe films on graphene/SiC. (a) STS (10 mV, 0.1 nA) on the center of a vortex core. (b) Zero bias conductance map (10 mV, 0.1 nA) for a single vortex at a 0.4 K and 1 T magnetic field. (c), (d) Tunneling conductance spectra measured at an equally spaced (2 nm) distance along the *a* and *b* axes, respectively.

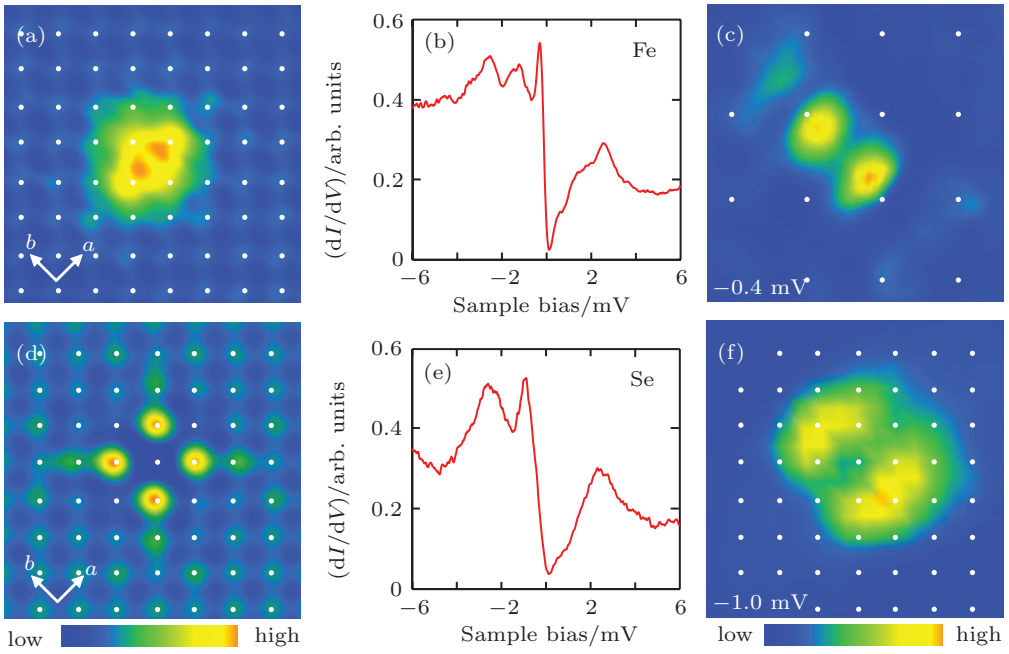


Fig. 8. Impurity-induced bound states in the superconducting gap of FeSe films on graphene/SiC. (a) STM topography (10 mV, 0.1 nA), (b) tunneling conductance spectrum (0.4 K, 10 mV, 0.1 nA), and (c) density of states map (−0.4 mV, 0.1 nA) of a single Fe adatom. (d) STM topography (10 mV, 0.1 nA), (e) tunneling conductance spectrum (0.4 K, 10 mV, 0.1 nA), and (f) density of states map (−1.0 mV, 0.1 nA) of a single Se vacancy. The white dots indicate the topmost Se atoms.

3.2. Thickness-dependent T_C

To reveal the two-dimensional superconductivity properties, STS studies were performed on thinner films. Figure 9(a) summarizes a series of normalized tunneling spectra taken on an 8-UC FeSe film at various temperatures. At 3.0 K, the superconducting gap with two symmetric coherence peaks at ±2.1 meV is clearly visible. With increasing temperature, both coherence peaks are suppressed, and the zero-bias conductance (ZBC) continuously increases until the gap completely disappears at 8.0 K. Using the tunneling spectra near T_C, ZBC shows a linear dependence on temperature (the inset of Fig. 9(a)). By extrapolating T_C to the point where ZBC = 1,

we find a T_C of 7.8 K for the 8-UC film. Similarly, we can determine the T_C of other films, for example, 3.7 K for the 2-UC film (Fig. 9(b)). In the 1-UC film, however, the observed gap near E_F is temperature independent, and it exhibits significant spatial inhomogeneity. This suggests that the 1-UC FeSe film is non-superconductive above 2.2 K.

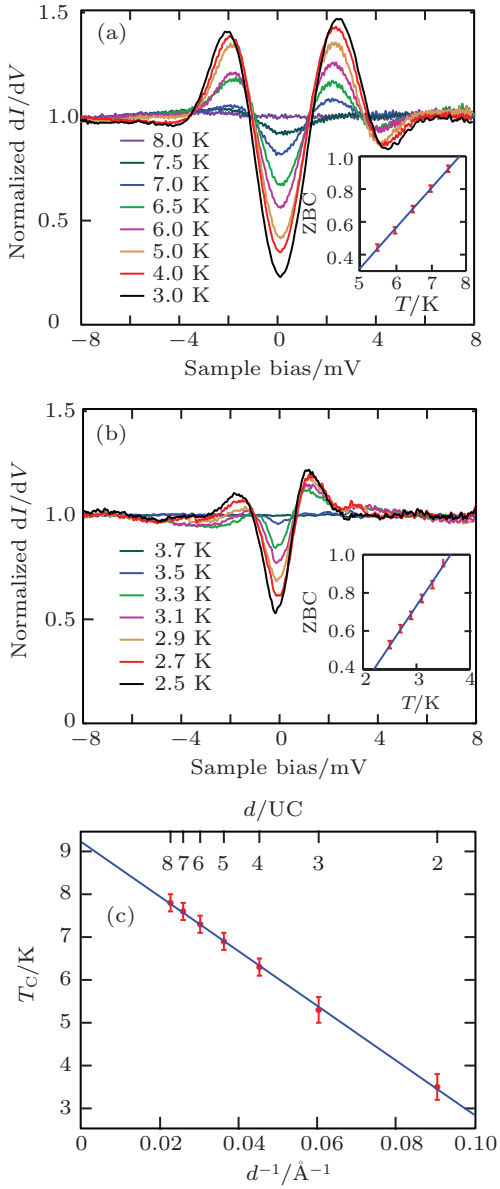


Fig. 9. Thickness dependence of tunneling conductance spectra in FeSe films on graphene/SiC. Panels (a) and (b) show a series of normalized tunneling conductance spectra on 8-UC and 2-UC FeSe films, respectively. Insets: temperature-dependent zero bias conductance. (c) Superconducting transition temperature T_C vs. the inverse of the film thickness d.

Figure 9(c) reveals the relationship between T_C and the inverse of the film thickness $1/d$. T_C scales inversely with film thickness d. As shown previously, for superconducting films, the transition temperature $T_C(d)$ is scaled as $T_C(d) = T_{C0}(1 - d_C/d)$, where $T_{C0}(d = \infty)$ is the critical temperature of the bulk, and d_C is the threshold for the onset of superconductivity. Theoretically, the $1/d$ dependence of T_C has generally been interpreted by adding a surface-energy term in the Ginzburg–Landau free energy of a superconductor.[45] Based on this relation, d_C is estimated to be 7 Å. In terms of the out-of-plane lattice constant of 5.518 Å for β-FeSe, this suggests that the minimum thickness for superconducting FeSe films is 2 UC, which is consistent with our experiment. Meanwhile, the extrapolation to infinite thickness ($1/d = 0$) yields $T_{C0} \approx 9.3$ K. This agrees well with the bulk T_C of the stoichiometric FeSe samples.

3.3. Suppression of superconductivity by twin boundaries

Twin boundaries (TBs) occur in the crystalline films. They are identified by the 90° rotation of the electronic dimers on either side and are seen roughly oriented along the diagonals of the Fe unit cells (Figs. 10(a) and 10(b)).[40] In all our topographic images, up to 1 eV, TBs appear brighter than the surrounding areas (Fig. 10(b)). This consistency over a wide energy range strongly suggests a local increase in h_{Se}.

Figure 10(c) summarizes a series of normalized tunneling conductance spectra taken along a trajectory approaching the twin boundary. All curves exhibit superconducting gaps with clear coherence peaks. However, the gap magnitude Δ decreases when approaching the TB. Moreover, the TB enhances the ZBC, which is inversely correlated with the superfluid density, and suppresses the coherence peaks. The above observations imply the suppression of superconductivity by the TBs in FeSe. Figure 10(d) presents the extracted superconducting gap Δ and ZBC from Fig. 10(c) as a function of distance d off the TB. As compared to $\Delta_0 = 2.2$ meV in TB-free regions, the superconducting gap shrinks by $\sim 25\%$ to $\Delta_{TB} = 1.66$ meV in the TBs. In addition, ZBC(d) decays with distance d from the TB as $\mathrm{ZBC}(d) = \mathrm{ZBC}(\infty) + A\exp(-d/\xi)$. Here, ZBC($\infty$) and ξ are the constant background and superconducting coherence length, respectively. Based on the exponential fitting, we extract a coherence length of $\xi = 5.5 \pm 0.3$ nm at 4.5 K. The coherence length $\xi(0) \sim 5.1$ nm at zero temperature can be calculated from the self-consistent BCS gap function and $\xi(T) \propto 1/\Delta(T)$ with $T_{C0} \approx 9.3$ K. Here, ξ is measured along one diagonal of the undistorted Fe unit cell, and thus $\xi(0) \sim 5.1$ nm roughly represents an average of ξ_a and ξ_b. Our STM images therefore demonstrate directly for the first time the coherence-length-scale effect of a TB on superconductivity in the new Fe-based superconductors.

Figure 11(a) shows a topographic image with three TBs. Figure 11(b) is the ZBC map recorded at 2 T, where the yellow regions with enhanced ZBC signify individual isolated vortices. The schematic depiction of vortices and TBs in Fig. 11(c) illustrates that the vortices are preferentially pinned on the TBs as long as the distance separating the neighboring TBs is not too large. This observation confirms that the TBs locally suppress the superconductivity in FeSe.

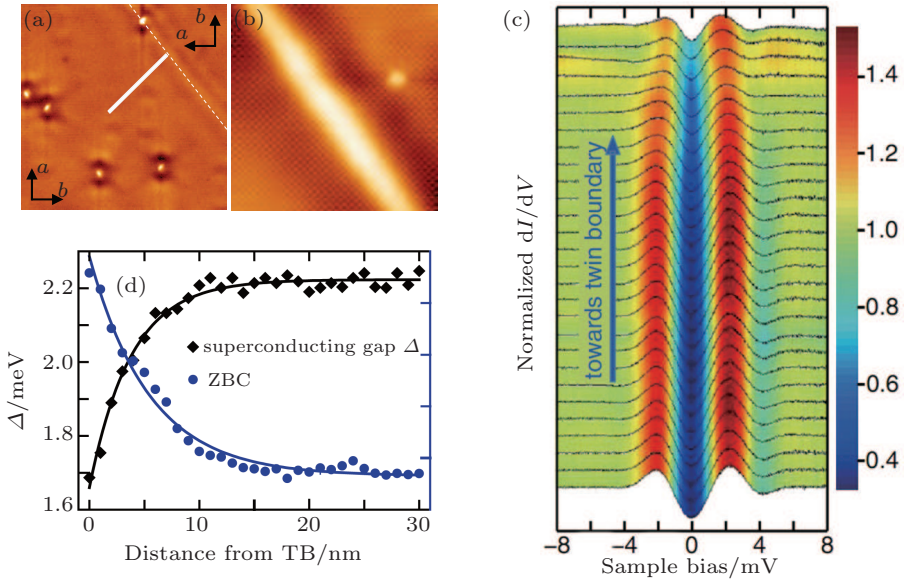


Fig. 10. STM characterization of twin boundaries in FeSe films on graphene/SiC. (a) STM topography with a TB indicated by a white dashed line (10 mV, 0.1 nA). (b) Atomic-resolution STM topography of a TB (10 mV, 43 pA). (c) Normalized tunneling conductance spectra taken at equal separations (1 nm) along the white solid line (normal to the TB) in panel (a). (d) Superconducting gap Δ and zero bias conductance plotted as a function of distance from the TB. The blue solid line depicts an exponential decay, while the black one is an eye-guide.

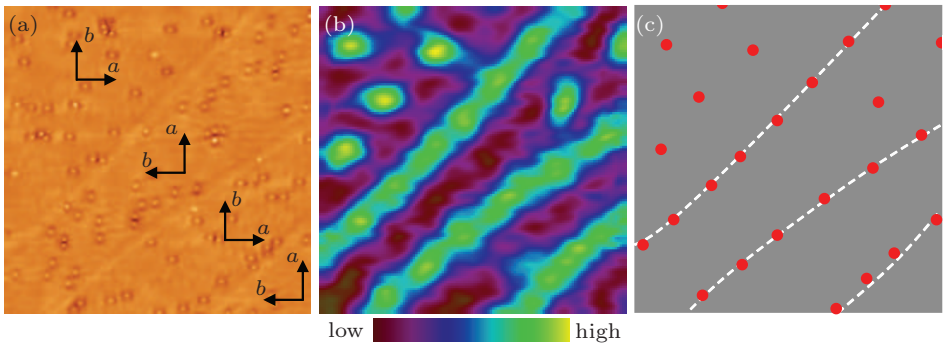


Fig. 11. Twin boundaries flux pinning. (a) A 150 nm×150 nm topographic image with three TBs (10 mV, 0.1 nA). (b) Simultaneous zero bias conductance map showing the vortices at 2 T (10 mV, 0.1 nA). (c) Schematic diagram illustrating both TBs (white dashes) and vortices (red circles).

In iron-based superconductors, the tetrahedral geometry, both the tetrahedral angle α and the anion height h_{anion} (pnictogen or chalcogen) above the Fe layer, appear to be key parameters controlling the superconducting transition temperature T_{C}.[17–20] Some previous studies have demonstrated that α does not significantly affect T_{C} in iron chalocogenides.[18,19] High-pressure electrical resistivity measurements have revealed that T_{C} increases as h_{Se} is reduced.[20] We suggest that superconductivity is suppressed and perhaps even quenched by the increased h_{Se} at the TB. The well-identified superconducting gaps near the TBs (Fig. 10(c)) may arise from the proximity effect between on- and off-TB regions.

As has been noted previously, the T_{C} of the iron-based superconductors appears to reach a maximum at $h_{\text{anion}} \sim 1.38$ Å.[17,20] Away from this value, T_{C} will abruptly decrease. In FeSe, $h_{\text{Se}} \sim 1.45$ Å> 1.38 Å,[20] so the increased h_{Se} must suppress T_{C} at the TBs. In contrast, in $Ba(Fe_{1-x}Co_x)As_2$, $h_{\text{As}} \sim 1.34$ Å appears smaller than 1.38 Å. Assuming that h_{As} increases around the TBs of $Ba(Fe_{1-x}Co_x)As_2$ as well, one can expect an enhanced superfluid density there, in line with SQUID experiments.[46,47] This suggests an explanation for the contrast between TB behaviors in FeSe and $Ba(Fe_{1-x}Co_x)As_2$, and therefore provides the first local evidence linking h_{anion} to the local Δ and thus to the mechanism of superconductivity in iron-based compounds.

4. High-temperature superconductivity at the FeSe/STO interface

Figure 12(a) shows the tunneling spectrum taken on the 1-UC FeSe film on STO (001) at 4.2 K. The 1-UC film exhibits an overall U-shaped conductance spectrum: a zero conductance region near E_{F} and an unusually large superconductive gap $\Delta = 20.1$ meV defined by the distance between the

two sharp peaks. This value is almost one order of magnitude larger than $\Delta \sim 2.2$ meV for bulk FeSe ($T_C = 9.3$ K). The ratio of $2\Delta/K_BT_C$ is ~ 5.5 (K_B is the Boltzmann constant) for bulk FeSe. If we assume the same superconducting mechanism for both the free-standing and epitaxial FeSe films, the gap of 1-UC FeSe must lead to a superconducting transition at ~ 80 K.

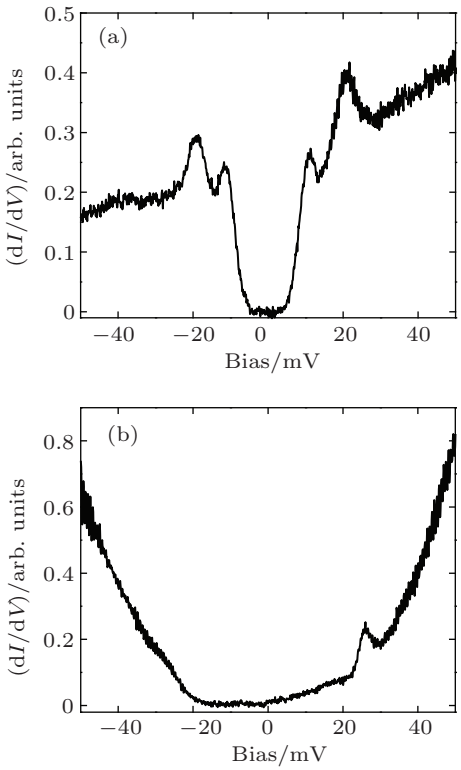


Fig. 12. Tunneling conductance spectra taken on FeSe films on STO (001). (a) Tunneling conductance spectrum taken on the 1-UC thick FeSe film revealing a superconducting gap of 20 meV. (b) Tunneling conductance taken on 2-UC thick FeSe films revealing a semiconductor-like behavior.

Surprisingly, the second UC and thicker films do not superconduct at all, and the observed superconductivity behavior is limited to the very first unit cell of the film above the interface. Shown in Fig. 12(b) is a tunneling spectrum taken on the 2-UC thick film. There is no superconducting gap, and its electronic structure near E_F is characterized by a semiconducting-like behavior. This feature is in sharp contrast to the free-standing FeSe films grown on graphene/SiC, where the T_C increases mostly with the increasing film thickness (Fig. 9(c)). The difference indicates that the FeSe/STO interface plays a significant role in the observed superconductivity.

The occurrence of superconductivity in the 1-UC FeSe film on STO is further confirmed by the presence of superconducting vortices under an external magnetic field at 4.2 K. Figure 13(a) shows the ZBC spectral mapping of a surface region shown in Fig. 13(b), where a vortex is clearly observed. Figure 13(c) displays a series of tunneling spectra taken at the points indicated by the dots in Fig. 13(a). With increasing distance from the vortex center, the coherent peaks gradually fade away, while the gap size remains unchanged.

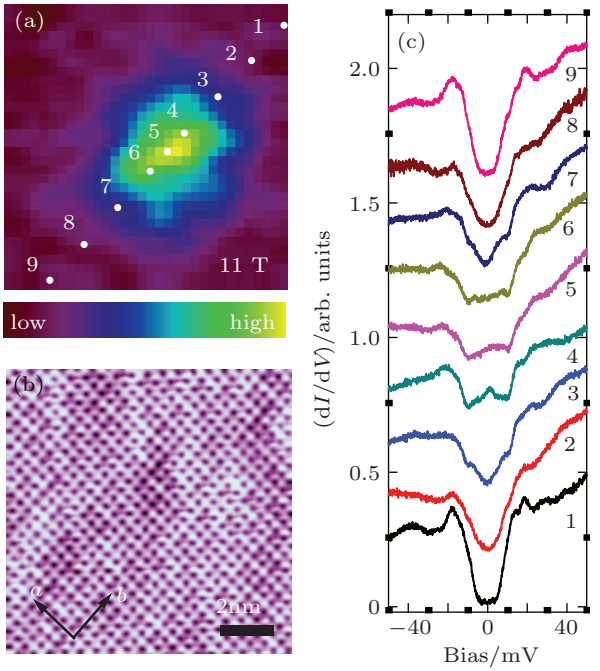


Fig. 13. Vortex core states in FeSe films on STO (001). (a) Zero-bias differential conductance mapping of the vortex state under a magnetic field at 4.2 K. (b) Simultaneously recorded STM topography of the mapping area shown in panel (a). (c) The tunneling conductance spectra taken on and near the vortex core indicated by the white points marked in panel (a). Near the vortex core center (points 4, 5, and 6), the superconducting coherence peaks at approximately ± 20 meV disappear, and bound states at E_F appear.

Ex situ macroscopic measurements also reveal the occurrence of superconductivity in the 1-UC FeSe film on STO. For example, *ex situ* transport measurement reveals the occurrence of superconducting transition with an onset temperature of 53 K;[41] *ex situ* angle resolved photoemission spectroscopy (ARPES) reveals a nearly isotropic superconducting gap of ~ 15 meV, which closes at a temperature of 65 ± 5 K,[48–50] a new record in T_C for iron-based superconductors.

While for the time being the mechanism for this high T_C superconductivity is not completely clear, we argue that the interface plays the dominant role. The interface could enhance the electron–phonon coupling[51] at the FeSe/TiO interface, as demonstrated in monolayer Pb and In films on Si (001) with a very similar structure.[38,52] In the present case, the effect may be further promoted by the polaronic effect associated with the high dielectric constant of STO.

5. Phase separation and magnetic order in $K_xFe_{2-y}Se_2$

The newly discovered alkali-doped iron selenide superconductors not only reach a superconducting transition tem-

perature as high as 33 K,[32] but also exhibit unique characteristics that are absent in other iron-based superconductors, such as antiferromagnetically ordered insulating phases[23,24] and the presence of Fe vacancies and ordering.[25–28] These features have generated considerable excitement as well as confusion, regarding the delicate interplay between Fe vacancies, magnetism, and superconductivity.[29–31]

5.1. Phase separation in $K_xFe_{2-y}Se_2$

Figures 14(a) and 14(b) show the tunneling conductance spectra at 0.4 K of regions I and II in Fig. 3(a), i.e., the stoichiometric KFe_2Se_2 and the $K_2Fe_4Se_5$ with a $\sqrt{5} \times \sqrt{5}$ ordered pattern of Fe vacancies in the films grown on graphene/SiC, respectively. The spectrum of stoichiometric KFe_2Se_2 (Fig. 14(a)) exhibits a superconducting gap centered at the Fermi energy and two characteristic coherence peaks, indicating a superconducting phase. It has a double-gap structure: a larger gap $\Delta_1 = 4$ meV and a smaller one $\Delta_2 \sim 1$ meV. In contrast, the spectrum of the $\sqrt{5} \times \sqrt{5}$ ordered pattern of Fe vacancies (Fig. 14(b)) exhibits an energy gap up to 0.43 eV across the Fermi level, suggesting an insulating phase.

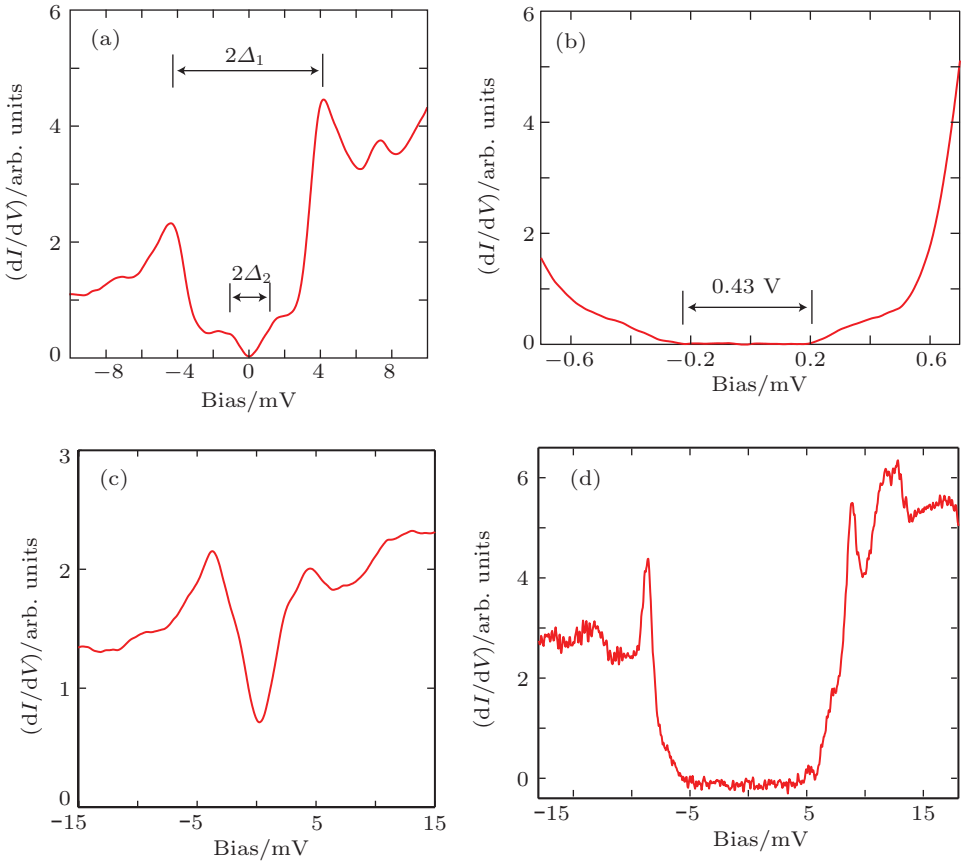


Fig. 14. Tunneling conductance spectra taken on $K_xFe_{2-y}Se_2$ films. (a), (b) Tunneling conductance spectra of regions I and II in Fig. 3(a), respectively. (c), (d) Tunneling conductance spectra of regions I and II in Fig. 4(b), respectively.

However, not all stoichiometric KFe_2Se_2 is superconducting. Shown in Figs. 14(c) and 14(d) are the tunneling conductance spectra of regions I and II in Fig. 4(b), i.e. the $\sqrt{2} \times \sqrt{2}$ phase and $\sqrt{2} \times \sqrt{5}$ phase in the stoichiometric KFe_2Se_2 films grown on STO, respectively. The spectrum of the $\sqrt{2} \times \sqrt{2}$ phase (Fig. 14(c)) shows a 10 mV dip near E_F. The dip may stem from the $\sqrt{2} \times \sqrt{2}$ charge ordering, but does not imply superconductivity because the bottom of the dip still has a finite density of states and the spectrum is essentially independent of temperature from 0.4 K to 4.2 K. Therefore, the $\sqrt{2} \times \sqrt{2}$ phase is a nonsuperconductive metal. The spectrum of the $\sqrt{2} \times \sqrt{5}$ phase (Fig. 14(d)) exhibits a full energy gap centered at the Fermi level and two pronounced coherence peaks, indicating that the $\sqrt{2} \times \sqrt{5}$ phase is superconducting with a nearly isotropic gap. The superconducting gap $\Delta = 8.8$ meV is estimated by half of the energy between the two coherence peaks and is in close agreement with that obtained by angle-resolved photoemission spectroscopy.[53–57]

Considering the surface structure shown in Fig. 5, we demonstrate that the nonsuperconductive phase of KFe_2Se_2

has $\sqrt{2}\times\sqrt{2}$ charge ordering, which becomes superconducting only when it interfaces with $K_2Fe_4Se_5$ and develops $\sqrt{2}\times\sqrt{5}$ charge ordering. Therefore, it is appropriate to identify KFe_2Se_2 with $\sqrt{2}\times\sqrt{2}$ charge ordering as the parent compound. There are various ways, such as strain, magnetic coupling, and charge transfer, with which the electronic properties of KFe_2Se_2 can be regulated through the $K_2Fe_4Se_5$ layer. The strain effect can simply be excluded because the lattice constants of $K_2Fe_4Se_5$ are very close to those of KFe_2Se_2. An analogy to cuprate high T_C superconductors suggests that the $K_2Fe_4Se_5$ layer may play the role of charge reservoir and transfer carriers into KFe_2Se_2 to induce superconductivity. To keep the balance of chemical valence, the KFe_2Se_2 phase tends to lose electrons and becomes hole-doped in the superconducting state. Another possibility is that the antiferromagnetic $K_2Fe_4Se_5$ may change the magnetic structure of KFe_2Se_2 through their exchange coupling across the interface, and KFe_2Se_2 becomes superconducting after the original C_4 symmetry is broken by the magnetic interaction. In all scenarios, the interface between KFe_2Se_2 and $K_2Fe_4Se_5$ is a key factor.

Interfacing with $K_2Fe_4Se_5$ is not the only way to induce superconductivity in the parent compound KFe_2Se_2. Superconductivity can also occur in a film with a certain amount of Se vacancies. The atomically resolved STM image in Fig. 15(a) shows the same $\sqrt{2}\times\sqrt{2}$ superstructure as the parent compound but with quatrefoil-like defects originating from the Se vacancies, where no sign of the $\sqrt{5}\times\sqrt{5}$ Fe vacancy order has been observed. The spectrum (Fig. 15(b)) at a location away from the Se vacancies exhibits a very similar superconducting gap to that on KFe_2Se_2 with $\sqrt{2}\times\sqrt{5}$ charge ordering (Fig. 14(d)).

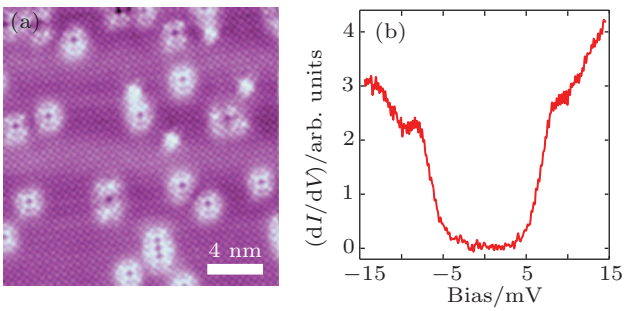


Fig. 15. Superconductivity in KFe_2Se_{2z}. (a) The STM topography (75 mV, 0.02 nA) of an area with Se vacancies. (b) The superconducting gap (0.4 K, 25 mV, 0.1 nA) at a location away from the Se vacancies.

Therefore, in total, four phases have been found to exist in $K_xFe_{2-y}Se_{2-z}$: parent compound KFe_2Se_2, superconducting KFe_2Se_2 with $\sqrt{2}\times\sqrt{5}$ charge ordering, superconducting KFe_2Se_{2-z} with Se vacancies, and insulating $K_2Fe_4Se_5$ with a $\sqrt{5}\times\sqrt{5}$ Fe vacancy order.

5.2. Magnetic order in $K_xFe_{2-y}Se_2$

Figure 16(a) shows an atomically resolved STM image of stoichiometric KFe_2Se_2 grown on graphene/SiC, where the topmost layer remains perfect without K or Se vacancies but with single Fe vacancies (parallelogram-shaped structures) in the second atomic layer. By examining the registration of Fe sites with respect to the Se lattice in the topmost layer, the Fe atoms in the (110) plane can be divided into two interpenetrating sublattices. The Fe vacancies on the two different sublattices are labeled as A and B. The atomic structures, chemical environments, and STM images of these two types of vacancies are mirror-images of each other. The tunneling conductance spectrum on a vacancy (Fig. 16(b)) shows strongly suppressed coherence peaks and a pair of resonances inside the superconducting gap, i.e., an electron-like bound state at 1.9 mV and a hole-like bound state at −1.9 mV. While the energies of the electron-like and hole-like states are symmetric with respect to zero bias, their amplitudes are different as a result of the on-site Coulomb interaction.[36]

When a magnetic field perpendicular to the sample surface is applied to break the rotational symmetry, as clearly shown in Figs. 16(c) and 16(d), the energy of the subgap resonance in KFe_2Se_2 exhibits a linear dependence on the magnetic field. The most striking behavior of the field effect is that the peaks on type-A and type-B vacancies shift to opposite directions with the magnetic field. The opposite shifting suggests that the two types of vacancies have different spin orientations, implying a magnetically-related bipartite order in the tetragonal Fe lattice. The bipartite spin structure is influenced by the applied magnetic field only slightly because of the relatively strong anti-ferromagnetic exchange coupling between neighboring spins. Such a bipartite structure may account for the large electron-like Fermi surface sheet with weak intensity near the Γ point in ARPES data[55,56] through Brillouin zone folding.

The role of the Fe vacancies in the superconducting phase has been rather controversial in previous studies. For example, some experimental data suggested that randomly distributed vacancies may help to stabilize the superconducting state.[31] To further elucidate the effect of the Fe vacancies on superconductivity, we prepared samples with a higher density of randomly distributed vacancies (Fig. 17(a)) by UHV annealing. The tunneling conductance spectra in Fig. 17(b) show that a sample with a high density of vacancies eventually becomes a gapless superconductor. Therefore, the Fe vacancies are always destructive to superconductivity in KFe_2Se_2.

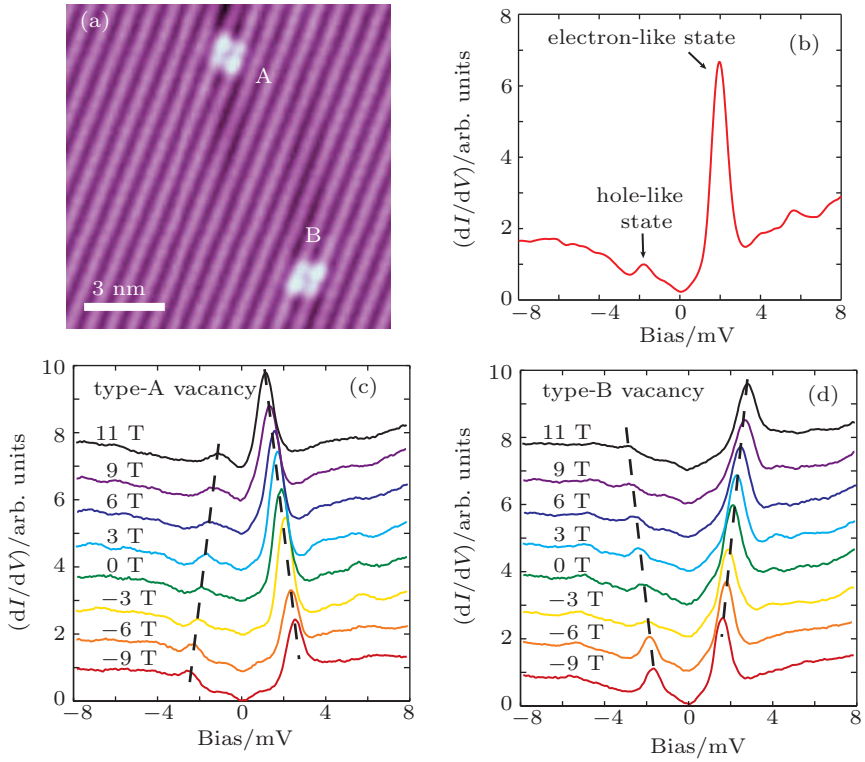


Fig. 16. Fe vacancy-induced bound states in the superconducting gap of KFe_2Se_2. (a) STM topography of Fe vacancies (30 mV, 0.03 nA). The two types of vacancies are labeled A and B, respectively. (b) Tunneling conductance spectrum (0.4 K, 15 mV, 0.1 nA) on a single Fe vacancy. (c), (d) Magnetic field dependences of the bound state energies.

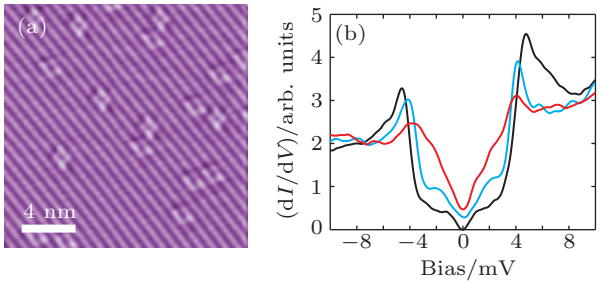


Fig. 17. Suppression of the superconductivity of KFe_2Se_2 by Fe vacancies. (a) STM topography (60 mV, 0.02 nA) of an area with a high density of Fe vacancies. (b) Superconducting gaps (15 mV, 0.1 nA) at various densities of vacancies: black curve: no vacancy; cyan curve: low density (0.05/nm^2) of vacancies; red curve: high density (0.1/nm^2) of vacancies, as shown in panel (a).

6. Summary

We successfully prepared stoichiometric and superconducting FeSe and $K_xFe_{2-y}Se_2$ films on graphene/SiC and STO (001) substrates using MBE. By *in situ* low-temperature STM study, which combines the capabilities of local imaging and a direct probe of the superconducting parameters at the nanometer scale, we clarified several issues of confusion, such as pairing symmetry and the interplay between magnetism and superconductivity in iron-based superconductors. The most important finding is the interface-induced high-temperature superconductivity. The main conclusions are as follows.

1) Graphene grown on SiC (0001) substrates can lead to the growth of strain-free FeSe films. The superconductivity transition temperature T_C of the FeSe films ($>$ 2 UC) scales inversely with the film thickness.

2) TBs locally suppress the superconductivity in FeSe. This is due to the increased h_{Se} at the FeSe TBs, which provides the first local evidence for the importance of chalcogen/pnictogen height h_{anion} to the nature of the superconductivity mechanism in iron-based materials.

3) We confirmed the nodal superconductivity and the twofold symmetry of the order parameter in FeSe films.

4) We discovered high-temperature superconductivity in 1-UC thick FeSe films grown on STO (001), which is induced by the interface effect. This finding not only demonstrates a powerful way for finding new superconductors and for raising T_C, but also provides a well-defined platform for systematic studies of the mechanism of unconventional superconductivity.

5) A $K_xFe_{2-y}Se_{2-z}$ sample contains four distinct phases: parent compound KFe_2Se_2, superconducting KFe_2Se_2 with $\sqrt{2}\times\sqrt{5}$ charge ordering, superconducting KFe_2Se_{2-z} with Se vacancies, and insulating $K_2Fe_4Se_5$ with a $\sqrt{5}\times\sqrt{5}$ Fe vacancy order.

6) An individual Fe vacancy can locally destroy superconductivity in a way similar to the effect of a magnetic impurity in the conventional superconductors. This finding elucidates the existing controversies on this new superconductor

and provides atomistic information on the interplay between magnetism and superconductivity in iron-based superconductors.

References

[1] Kamihara Y, Watanabe T, Hirano M and Hosono H 2008 *J. Am. Chem. Soc.* **130** 3296

[2] Rotter M, Tegel M and Johrendt D 2008 *Phys. Rev. Lett.* **101** 107006

[3] Wang X C, Liu Q Q, Lü Y X, Gao W B, Yang L X, Yu R C, Li F Y and Jin C Q 2008 *Solid State Commun.* **148** 538

[4] Ren Z A, Lu W, Yang J, Yi W, Shen X L, Li Z C, Che G C, Dong X L, Sun L L, Zhou F and Zhao Z X 2008 *Chin. Phys. Lett.* **25** 2215

[5] Ishida K, Nakaii Y and Hosono H 2009 *J. Phys. Soc. Jpn.* **78** 062001

[6] Zhu X, Han F, Mu G, Cheng P, Shen B, Zeng B and Wen H 2009 *Phys. Rev. B* **79** 220512

[7] Paglione J and Greene R L 2010 *Nat. Phys.* **6** 645

[8] Hsu F C, Luo J Y, The K W, Chen T K, Huang T W, Wu P M, Lee Y C, Huang Y L, Chu Y Y, Yan D C and Wu M K 2008 *Proc. Nat. Acad. Sci. USA* **105** 14262

[9] Mizuguchi Y, Tomioka F, Tsuda S, Yamaguchi T and Takano Y 2008 *Appl. Phys. Lett.* **93** 152505

[10] Medvedev S, McQueen T M, Troyan I A, Palasyuk T, Eremets M I, Cava R J, Naghavi S, Casper F, Ksenofontov V, Wortmann G and Felser C 2009 *Nat. Mater.* **8** 630

[11] Lee S H, Xu G Y, Ku W, Wen J S, Lee C C, Katayama N, Xu Z J, Ji S, Lin Z W, Gu G D, Yang H B, Johnson P D, Pan Z H, Valla T, Fujita M, Sato T J, Chang S, Yamada K and Tranquada J M 2010 *Phys. Rev. B* **81** 220502

[12] Argyriou D N, Hiess A, Akbari A, Eremin I, Korshunov M M, Hu J, Qian B, Mao Z Q, Qiu Y M, Broholm C and Bao W 2010 *Phys. Rev. B* **81** 220503

[13] Mook H A, Lumsden M D, Christianson A D, Nagler S E, Sales B C, Jin R Y, McGuire M A, Sefat A S, Mandrus D, Egami T and Cruz C D 2010 *Phys. Rev. Lett.* **104** 187002

[14] Lumsden M D, Christianson A D, Goremychkin E A, Nagler S E, Mook H A, Stone M B, Abernathy D L, Guidi T, MacDougall G J, Cruz C D, Sefat A S, McGuire M A, Sales B C and Mandrus D 2010 *Nat. Phys.* **6** 182

[15] Babkevich P, Bendele M, Boothroyd A T, Conder K, Gvasaliya S N, Khasanov R, Pomjakushina E and Roessli B 2010 *J. Phys.: Condens. Matter* **22** 142202

[16] Lumsden M D and Christianson A D 2010 *J. Phys.: Condens. Matter* **22** 203203

[17] Johnston D C 2010 *Adv. Phys.* **59** 803

[18] Huang S X, Chien C L, Thampy V and Broholm C 2010 *Phys. Rev. Lett.* **104** 217002

[19] Horigane K, Hiraka H and Ohoyama K 2009 *J. Phys. Soc. Jpn.* **78** 074718

[20] Okabe H, Takeshita N, Horigane K, Muranaka T and Akimitsu J 2010 *Phys. Rev. B* **81** 205119

[21] Guo J G, Jin S F, Wang G, Wang S C, Zhu K X, Zhou T T, He M and Chen X L 2010 *Phys. Rev. B* **82** 180520

[22] Wang A F, Ying J J, Yan Y J, Liu R H, Luo X G, Li Z Y, Wang X F, Zhang M, Ye G J, Cheng P, Xiang Z J and Chen X H 2011 *Phys. Rev. B* **83** 060512

[23] Fang M H, Wang H D, Dong C H, Li Z J, Feng C M, Chen J and Yuan H Q 2011 *Europhys. Lett.* **94** 27009

[24] Chen Z G, Yuan R H, Dong T, Xu G, Shi Y G, Zheng P, Luo J L, Guo J G, Chen X L and Wang N L 2011 *Phys. Rev. B* **83** 220507

[25] Wang Z, Song Y J, Shi H L, Wang Z W, Chen Z, Tian H F, Chen G F, Guo J G, Yang H X and Li J Q 2011 *Phys. Rev. B* **83** 140505

[26] Zavalij P, Bao W, Wang X F, Ying J J, Chen X H, Wang D M, He J B, Wang X Q, Chen G F, Hsieh P Y, Huang Q and Green M A 2011 *Phys. Rev. B* **83** 132509

[27] Yan X W, Gao M, Lu Z Y and Xiang T 2011 *Phys. Rev. B* **83** 233205

[28] Ricci A, Poccia N, Campi G, Joseph B, Arrighetti G, Barba L, Reynolds M, Burghammer M, Takeya H, Mizuguchi Y, Takano Y, Colapietro M, Saini N L and Bianconi A 2011 *Phys. Rev. B* **84** 060511

[29] Shermadini Z, Krzton-Maziopa A, Bendele M, Khasanov R, Luetkens H, Conder K, Pomjakushina E, Weyeneth S, Pomjakushin V, Bossen O and Amato A 2011 *Phys. Rev. Lett.* **106** 117602

[30] Bao W, Li G N, Huang Q Z, Chen G F, He J B, Wang D M, Green M A, Qiu Y M, Luo J L and Wu M M 2013 *Chin. Phys. Lett.* **30** 027402

[31] Shen B, Zeng B, Chen G F, He J B, Wang D M, Yang H and Wen H H 2011 *Europhys. Lett.* **96** 37010

[32] Mizuguchi Y, Takeya H, Kawasaki Y, Ozaki T, Tsuda S, Yamaguchi T and Takano Y 2011 *Appl. Phys. Lett.* **98** 042511

[33] Cai P, Ye C, Ruan W, Zhou X D, Wang A F, Zhang M, Chen X H and Wang Y Y 2012 *Phys. Rev. B* **85** 094512

[34] Yazdani A, Jones B A, Lutz C P, Crommie M F and Eigler D M 1997 *Science* **275** 1767

[35] Ji S H, Zhang T, Fu Y S, Chen X, Ma X C, Li J, Duan W H, Jia J F and Xue Q K 2008 *Phys. Rev. Lett.* **100** 226801

[36] Balatsky A V, Vekhter I and Zhu J X 2006 *Rev. Mod. Phys.* **78** 373

[37] Fischer Ø, Kugler M, Maggio-Aprile I, Brthod C and Renner C 2007 *Rev. Mod. Phys.* **79** 353

[38] Zhang T, Cheng P, Li W J, Sun Y J, Wang G, Zhu X G, He K, Wang L L, Ma X C, Chen X, Wang Y Y, Liu Y, Lin H Q, Jia J F and Xue Q K 2010 *Nat. Phys.* **6** 104

[39] Song C L, Wang Y L, Jiang Y P, Li Z, Wang L L, He K, Chen X, Ma X C and Xue Q K 2011 *Phys. Rev. B* **84** 020503

[40] Song C L, Wang Y L, Cheng P, Jiang Y P, Li W, Zhang T, Li Z, He K, Wang L L, Jia J F, Hung H H, Wu C J, Ma X C, Chen X and Xue Q K 2011 *Science* **332** 1410

[41] Song C L, Wang Y L, Jiang Y P, Wang L L, He K, Chen X, Hoffman J E, Ma X C and Xue Q K 2012 *Phys. Rev. Lett.* **109** 137004

[42] Wang Q Y, Li Z, Zhang W H, Zhang Z C, Zhang J S, Li W, Ding H, Ou Y B, Deng P, Chang K, Wen J, Song C L, He K, Jia J F, Ji S H, Wang Y Y, Wang L L, Chen X, Ma X C and Xue Q K 2012 *Chin. Phys. Lett.* **29** 037402

[43] Li W, Ding H, Deng P, Chang K, Song C L, He K, Wang L L, Ma X C, Hu J P, Chen X and Xue Q K 2011 *Nat. Phys.* **8** 126

[44] Li W, Ding H, Li Z, Deng P, Chang K, He K, Ji S H, Wang L L, Ma X C, Hu J P, Chen X and Xue Q K 2012 *Phys. Rev. Lett.* **109** 057003

[45] Kobayashi K 1996 *Phys. Rev. B* **53** 11091

[46] Simonin J 1986 *Phys. Rev. B* **33** 7830

[47] Kalisky B, Kirtley J R, Analytis J G, Chu J H, Vailionis A, Fisher I R and Moler K A 2010 *Phys. Rev. B* **81** 184513

[48] Kirtley J R, Kalisky B, Luan L and Moler K A 2010 *Phys. Rev. B* **81** 184514

[49] Liu D F, Zhang W H, Mou D X, He J F, Ou Y B, Wang Q Y, Li Z, Wang L L, Zhao L, He S L, Peng Y Y, Liu X, Chen C Y, Yu L, Liu G D, Dong X L, Zhang J, Chen C T, Xu Z Y, Hu J P, Chen X, Ma X C, Xue Q K and Zhou X J 2012 *Nature Commun.* **3** 931

[50] He S L, He J F, Zhang W H, Zhao L, Liu D F, Liu X, Mou D X, Ou Y B, Wang Q Y, Li Z, Wang L L, Peng Y Y, Liu Y, Chen C Y, Yu L, Liu G D, Dong X L, Zhang J, Chen C T, Xu Z Y, Chen X, Ma X C, Xue Q K and Zhou X J 2012 arXiv:1207.6823

[51] Tan S Y, Xia M, Zhang Y, Ye Z R, Chen F, Xie X, Peng R, Xu D F, Fan Q, Xu H C, Juan J, Zhang T, Lai X C, Xiang T, Hu J P, Xie B P and Feng D L 2013 arXiv:1301.2748

[52] Luh D A, Miller T, Paggel J J and Chiang T T 2002 *Phys. Rev. Lett.* **88** 256802

[53] Uchihashi T, Mishra P, Aono M and Nakayama T 2011 *Phys. Rev. Lett.* **107** 207001

[54] Zhang Y, Yang L X, Xu M, Ye Z R, Chen F, He C, Xu H C, Jiang J, Xie B P, Ying J J, Wang X F, Chen X H, Hu J P, Matsunami M, Kimura S and Feng D L 2011 *Nat. Mater.* **10** 273

[55] Qian T, Wang X P, Jin W C, Zhang P, Richard P, Xu G, Dai X, Fang Z, Guo J G, Chen X L and Ding H 2011 *Phys. Rev. Lett.* **106** 187001

[56] Zhao L, Mou D X, Liu S Y, Jia X W, He J F, Peng Y Y, Yu L, Liu X, Liu G D, He S L, Dong X L, Zhang J, He J B, Wang D M, Chen G F, Guo J G, Chen X L, Wang X Y, Peng Q J, Wang Z M, Zhang S J, Yang F, Xu Z Y, Chen C T and Zhou X J 2011 *Phys. Rev. B* **83** 140508

[57] Wang X P, Qian T, Richard P, Zhang P, Dong J, Wang H D, Dong C H, Fang M H and Ding H 2011 *Europhys. Lett.* **93** 57001

[58] Xu M, Ge Q Q, Peng R, Ye Z R, Jiang J, Chen F, Shen X P, Xie B P, Zhang Y, Wang A F, Wang X F, Chen X H and Feng D L 2012 *Phys. Rev. B* **85** 220504